Solid-State Electronics 77 (2012) 46–50

Contents lists available at SciVerse ScienceDirect

Solid-State Electronics

journal homepage: www.elsevier.com/locate/sse

Fabrication and characterization of carbon nanotube intermolecular p–n junctions

H. Li, Q. Zhang, C.C. Yap, B.K. Tay *

Microelectronics Center, School of Electrical and Electronics Engineering, Nanyang Technological University, Singapore 639798, Singapore

ARTICLE INFO

Article history:
Available online 31 July 2012

Keywords:
Carbon nanotubes
Intermolecular p–n junction
Transport mechanism

ABSTRACT

We demonstrate carbon nanotube intermolecular p–n junctions and study the electron transport mechanisms. Thermionic emission is the main transport mechanisms under forward bias while tunneling dominates the electron transport of the reverse bias condition. A kink point appearing on the plot of $\ln(I/V^2)$ versus $1/V$ indicates that the transport mechanism experiences a transition from direct tunneling to the Fowler–Nordheim tunneling under the reverse bias condition. In contrast, the Arrhenius plot of the I–V curve at forward biases suggests that tunneling is more important than the thermionic emission below 50 K.

1. Introduction

Carbon nanotube junctions (CNTJs) are of great significance for both fundamental research and nanoelectronic applications. The current rectifying characteristics of various CNTJs have been intensively studied. Zhou et al. implemented an intramolecular CNT p–n junction by chemical doping [1]. Lee and co-workers demonstrated a rectifying diode with intramolecular CNT p–n junction by electrostatic "doping" [2]. Fuhrer et al. fabricated a rectifying Schottky diode using an intermolecular CNTJ, which was randomly formed between a metallic and a semiconducting CNT [3]. Moreover, Y-shaped CNTJs also exhibit rectifying behavior because of an abrupt change in bandgap due to different tube diameters [4–6]. However, as most Y-shaped CNTJs are made of multi-walled CNTs, they have more complicated structures and less predictable electrical characteristics than that consists of single-walled CNT (SWCNT). On the contrary, an intramolecular CNT p–n junction by doping method could be fabricated in a more controllable manner [1,2]. Nevertheless, the doping profile in the intramolecular junctions is extremely difficult to control owing to the miniature size of the junction area. In comparison with the aforementioned two types of CNTJs, an intermolecular p–n junction consisting of a cross of p- and n-type SWCNTs has two apparent advantages (1) doping an entire SWCNT is an easily controllable process and (2) the junction obtained is abrupt owing to the sudden geometry change from p- to n-type SWCNT. Up till now, most of the cross CNTJs were fabricated by random formation [7–9] or atomic force microscopy (AFM) manipulation [10]. In this paper, we report on an SWCNT p–n junction that consists of a SWCNT cross fabricated using a controllable method. Moreover, the transport mechanisms in the p–n junction are investigated systematically.

2. Experimental

A 500-nm-thick SiO_2 layer was thermally grown on a heavily doped p-type ⟨100⟩ silicon substrate (boron as dopant, resistivity of 0.01–0.02 Ω cm). Metallic electrodes were fabricated using standard photolithography and lift-off process. The electrodes were made of titanium (5 nm) covered by gold (25 nm). SWCNTs were dispersed in deionized water with Triton × 100 ($C_{14}H_{22}O(C_2H_4O)_n$, where n is 9 or 10) as surfactants (1% by weight). Then, the suspension was ultrasonicated for 30 min (ultrasonic power ~27 W/L). An ac electric field (~1.2 V/μm) was applied between a pair of electrodes (S and S′ in Fig. 1a) using a function generator (SIN wave with frequency of 6 MHz), and then the nanotube suspension was dropped to cover the electric field region. After a CNT/bundle was confirmed to bridge the pair of electrodes by monitoring the resistance between the electrodes, the device was rinsed with deionized water and dried by nitrogen blowing. Subsequently, a 100-nm-thick Si_3N_4 layer was deposited at 300 °C and 40 W using PECVD at a deposition rate of 19 nm/min using a mixed flow gases of 100-sccm 10% silane gas (diluted by nitrogen gas), 20-sccm 99% ammonia gas and 600-sccm nitrogen gas. A pair of electrode pads D and D′ was prepared so that the bottom SWCNT was situated between them. Then, another SWCNT-bundle was bridged across D and D′ (see Fig. 1a). Finally, the Si_3N_4 layer at the cross point was etched away using wet etchant (hydrofluoride and deionized water with a volume ratio of 1:20 at the etch rate about 10 nm/s.) The resistance between D and S was monitored during etching to ensure the top and bottom SWCNTs contacted each other. The purpose of the Si_3N_4 layer was to electrically isolate bottom (S and S′) and top (D and D′) electrodes [11].

* Corresponding author.
E-mail address: ebktay@ntu.edu.sg (B.K. Tay).

0038-1101/$ - see front matter © 2012 Elsevier Ltd. All rights reserved.
http://dx.doi.org/10.1016/j.sse.2012.05.011

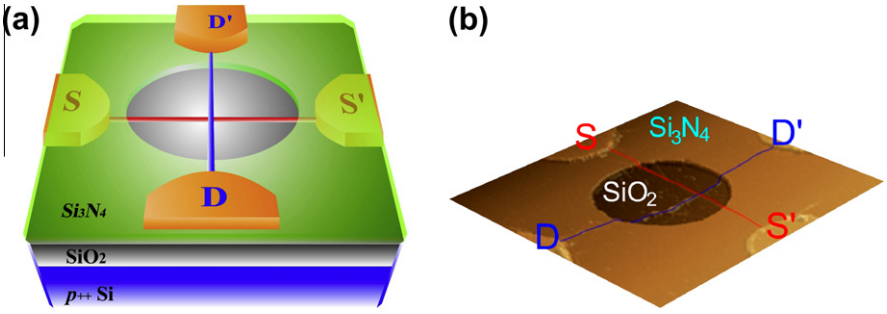

Fig. 1. Carbon nanotube intermolecular p–n junction. (a) A schematic device structure. (b) A false color AFM image. D–D′ and S–S′ delineate the top and bottom SWCNTs, respectively.

3. Results and discussion

Fig. 1b shows an AFM image of a typical device. The heavily doped Si substrate serves as the back-gate electrode. Fig. 2a presents the current of the top tube (T-SWCNT) $I_{DD'}$ measured at room temperature in air ambient and in a cryogenic chamber (pressure of 0.1 mbar), respectively. The T-SWCNT is p-type in air due to adsorbed oxygen molecules that dope holes to the tube [12–14] and/or modulate the work function of Au electrode (φ_{Au}). It remains an open question whether the doping or variation in φ_{Au} dominates the p-type conversion. Derycke et al. suggested that the change in φ_{Au} modulated the Schottky barrier at the metal/SWCNT contact [15]. In contrast, Ahn and co-workers measured the hole doping of SWCNT in air using scanning photocurrent microscopy, and found that the Fermi level moved close to the SWCNT valence band due to oxygen adsorption [14]. Compared to the transfer curve in air, the current of T-SWCNT decreases in the vacuum (red solid circle). The bottom tube (B-SWCNT) changes from p- to n-type after the Si_3N_4 layer is deposited. The conduction type change is caused by nearly completely desorption of oxygen when the device is heated up to 300 °C in high vacuum (10^{-5} mbar) during Si_3N_4 deposition [16,17]. After etching the Si_3N_4 layer, B-SWCNT turns back to p-

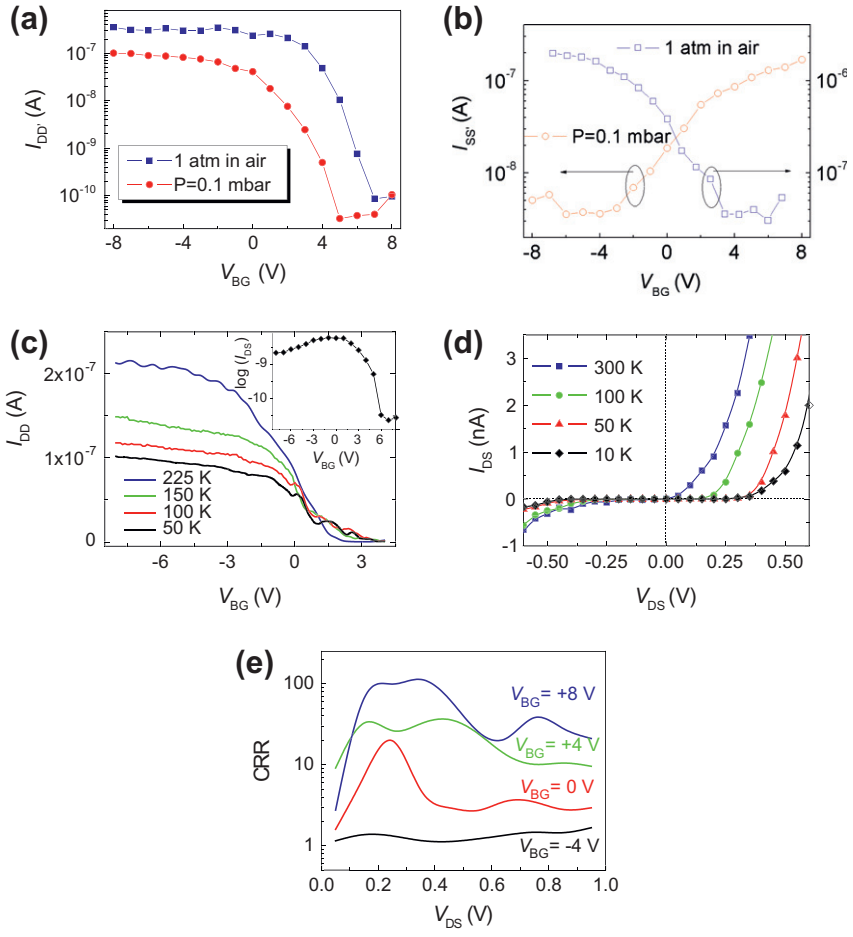

Fig. 2. Channel current ($I_{DD'}$) versus the back-gate voltage (V_{BG}) of the (a) T-SWCNT and (b) B-SWCNT at room temperature in air ambient and a vacuum of 0.1 mbar, respectively. (c) Transfer curves of the T-SWCNT at 50, 100, 150 and 225 K, respectively. Inset: Logarithmic plot of I_{DS}–V_{BG} with V_{DS} = 0.2 V at 300 K and 0.1 mbar. (d) I_{DS}–V_{DS} curves with V_{BG} = +4 V at 10, 50, 100 and 300 K, respectively. (e) Current rectification ratio (CRR) versus V_{DS} at V_{BG} = −4, 0, +4 and +8 V, respectively, at 300 K and 0.1 mbar.

type in air (blue open squares). Interestingly, it changes to n-type again in vacuum (red open circles), obviously due to partial oxygen desorption, as shown in Fig. 2b. The p- to n-type conversion of B-SWCNT could only be attributed to the hole doping level change, since the contacts of the B-SWCNT (S and S′) are passivated by the Si_3N_4 layer. The other evidence is that the threshold voltages of B-SWCNT change from +3 V (in air) to −4 V (in vacuum). Variation in φ_{Au} would not cause a significant change in the threshold voltage [15]. Therefore, hole doping is the dominant factor for the conduction type change in B-SWCNT, instead of variation in φ_{Au}. Nevertheless, the origin of different conduction type between T-SWCNT and B-SWCNT in vacuum is not clear. A tentative explanation can be twofold as follows. Firstly, the density of oxygen adsorption sites [18] on B-SWCNT may be much smaller than that of the T-SWCNT because B-SWCNT has gone through annealing and Si_3N_4 coating in PECVD. As a result, less oxygen molecules would adsorb on the surface of B-SWCNT than T-SWCNT in vacuum. Secondly, φ_{Au} of the top electrodes (D and D′) is higher than that of the bottom electrodes (S and S′) as a large number of oxygen molecules could still absorb on D and D′ electrodes even in vacuum (at room temperature).

The p-type conduction of T-SWCNT persists at low temperatures, as shown in Fig. 2c. However, the magnitudes of the current levels decrease at low temperatures probably due to the suppression of thermionic current component [19]. Thus, I_{DS} flows from D to S through a p–n CNTJ. The junction current also depends on V_{BG}, as shown in the inset. I_{DS} increases and then decreases when V_{BG} is swept from −8 to 8 V. The reason is that I_{DS} is determined by the smaller value between $I_{DD'}$ and $I_{SS'}$ since the p- and n-type SWCNTs are connected in series. The logarithmic plot of I_{DS} versus V_{BG} curve shows that the conductance of the p–n CNTJ can be modulated by V_{BG} with current ON/OFF ratio of 250. Fig. 2d shows the I_{DS}–V_{DS} curves at V_{BG} = +4 V at different temperatures from 10 to 300 K. Rectifying diode characteristics persist through the entire temperature range. I_{DS} increases sharply beyond a voltage threshold (50 mV at 300 K) under forward bias (FB), *i.e.*, D is positively biased with respect to S. The appearance of a voltage threshold is consistent with a built-in electrical field at the interface between the B-SWCNT and T-SWCNT. In contrast, I_{DS} is blocked under reverse bias (RB), *i.e.*, S is positively biased respect to D. The rectifying diode behavior can be quantitatively described using current rectification ratio (CRR), which is defined as the relative change in I_{DS} when V_{DS} is reversed [20], *i.e.*, $I_{DS}(V_{DS})/I_{DS}(-V_{DS})$ (see Fig. 2e). CRR can be as high as 100 and becomes higher at a large positive V_{BG}, indicating the rectifying diode behavior is more pronounced when the device is approaching OFF state. It is noted that the current rectification characteristics are not as significant as that in an intramolecular p–n CNTJ [2]. The reason could be the junction barrier, which is caused by the nanoscale air gap between tubes [21] and/or absorbents on the surface of the nanotubes [22], blocks the electronic carrier transport under both FB and RB. As a result, the influence of built-in potential on current rectification is weakened.

The Arrhenius plot (see Fig. 3a) under FB shows evidently a linear regime (T > 50 K) and a nonlinear regime (T < 50 K), consistent with the thermionic emission and tunneling process, respectively. The extracted activation energy E_a can be extracted from the temperature-dependent thermionic emission current ($I_{DS} \propto \exp(-\frac{qE_a}{kT})$ where q is the elementary charge and k is Boltzmann constant). E_a as a function of $\sqrt{V_{DS}}$ is depicted in Fig. 3b. One can see that the activation energy decreases with increasing $\sqrt{V_{DS}}$ [23]. This could suggest that the forward bias voltage partially compensates the built-in potential and hence reduces the activation energy barrier. As displayed in Fig. 3b, the activation energy in the absence of bias voltage is extrapolated to be about 100 meV [23,24]. A closer look at the temperature dependences of the I–V curves reveals that different transport mechanisms dominate various V_{DS} regions. The inset of Fig. 3b presents the slopes of the linear portion of the log I_{DS}–V_{DS} curves, *i.e.*, $S = \Delta \log I_{DS}/\Delta V_{DS}$, under the small FB (S-FB), large FB (L-FB) and RB, respectively. It is worth noting that the slope under S-FB (V_{DS} < 0.4 V) decreases significantly from 16 dec/V at 50 K to 6 dec/V at 300 K (open diamonds). The significant temperature dependence of the slope ascribes the carrier transport to thermionic emission, consistent with Fig. 3a. The slope at 10 K (circle) does not increase linearly with respect to that at 50 K. This could indicate that the tunneling current component dominates at T < 50 K [19]. In contrast, the slopes under RB and L-FB (V_{DS} > 0.4 V) remain almost unchanged around 4 dec/V (open circles) and 1.5 dec/V (open squares), respectively. The temperature-independent slope attributes the carrier transport to tunneling [25]. Under FB, the built-in potential is partially counterbalanced by the bias voltage V_{DS}. The majority of the holes injected from D have enough energy to thermionically emit over the junction barrier. The thermal energy of those holes decreases as temperature is reduced. Thus, tunneling through the junction barrier still plays an important role below 50 K, as suggested by the saturated slope (circle) in the inset of Fig. 3b. Moreover, the influence of V_{BG} on the energy bands can be understood as follows. The larger current of T-SWCNT compared to that of B-SWCNT at zero V_{BG} suggests the p-type doping is stronger than the n-type doping (see Fig. 2a and b). In other words, the hole concentration in p-type SWCNT is larger than the electron concentration in n-type SWCNT in the absence of V_{BG}. As a consequence, varying V_{BG} is less effective to move the Fermi level in p-type SWCNT than that in n-type. For instance, the Fermi level moves towards the valence bands when V_{BG} is decreased from 0 to −4 V. But the Fermi level in n-type SWCNT moves farther than that in p-type SWCNT due to the smaller carrier concentration in n-type SWCNT. As a consequence, the built-in potential is reduced effectively. Similarly, the built-in potential increases effectively when V_{BG} increases from 0 to +4 V. A higher built-in potential at V_{BG} = +4 V results in a larger CRR in comparison with the condition of −4 V. This explains the observation of larger CRR at more positive V_{BG} in Fig. 2e.

We now come to discuss the RB region. Simmons proposed that the current tunneling through an arbitrary shaped molecular junction can be expressed as [26]:

$$I_{bias} = \frac{qA}{4\pi^2\hbar d^2}\left\{\left(\phi - \frac{qV_{bias}}{2}\right)\exp\left(-\frac{2d\sqrt{2m_e}}{\hbar}\sqrt{\phi - \frac{qV_{bias}}{2}}\right) - \left(\phi + \frac{qV_{bias}}{2}\right)\exp\left(-\frac{2d\sqrt{2m_e}}{\hbar}\sqrt{\phi + \frac{qV_{bias}}{2}}\right)\right\} \quad (1)$$

where A is the molecular junction area, d is the barrier width, m_e is the electron effective mass and φ is the barrier height. With a rectangular barrier at a low bias, Eq. (1) is reduced to $\ln\left(\frac{I_{bias}}{V_{bias}^2}\right) \propto \ln\left(\frac{1}{V_{bias}}\right) - \frac{2d\sqrt{2m_e\phi}}{\hbar}$. In contrast, for a triangular barrier at a high bias, Eq. (1) is simplified as $\ln\left(\frac{I_{bias}}{V_{bias}^2}\right) \propto \left(\frac{1}{V_{bias}}\right)\frac{4d\sqrt{2m_e\phi^3}}{3\hbar q}$. Thus, from the plot of $\ln\left(\frac{I_{bias}}{V_{bias}^2}\right)$ versus $\frac{1}{V_{bias}}$, one can differentiate the transport governed by direct tunneling (through a rectangular barrier) from Fowler–Nordheim (F–N) tunneling (through a triangular barrier). Interestingly, the current transport through the intermolecular CNT p–n junction also follows the Simmons model [24,27]. To identify the detailed tunneling mechanism, the plot of $\ln\left(\frac{I_{DS}}{V_{DS}^2}\right) - \frac{1}{V_{DS}}$ at 50, 100 and 300 K are shown in Fig. 3c, respectively. A linear (left) and a nonlinear (right) regime separated by a transition voltage ($V_t \sim 0.13$ V) are observed (open symbols). The calculated curves (solid lines) based on $\ln\left(\frac{I_{DS}}{V_{DS}^2}\right) \propto \left(\frac{1}{V_{DS}}\right)$ and

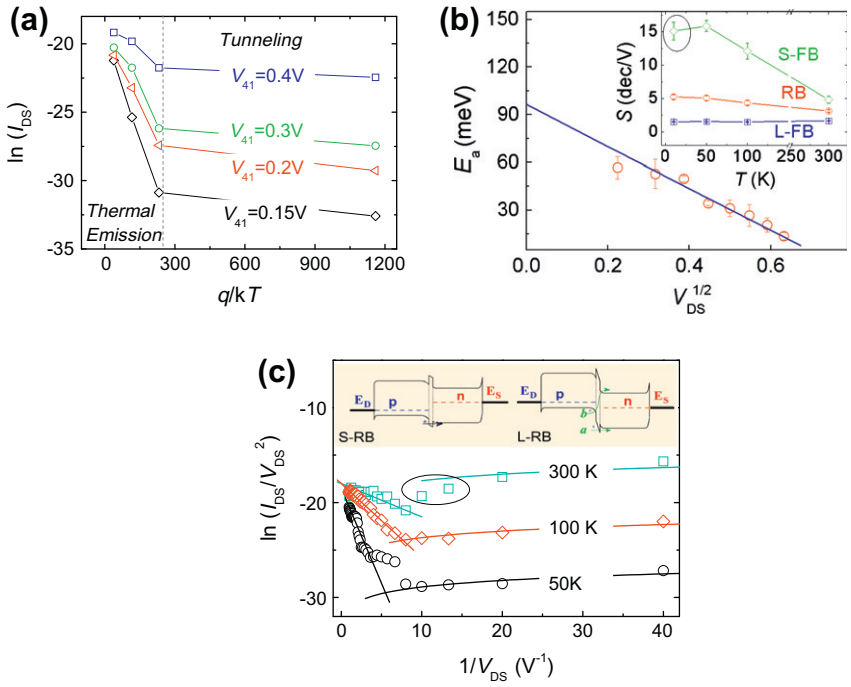

Fig. 3. (a) Arrhenius plot of I_{DS} under small FB. Thermionic emission and tunneling regimes were observed with transition temperature at 50 K. (b) Activation energy E_a versus $\sqrt{V_{DS}}$. Inset: slope (S) of log I_{DS} versus T with V_{BG} = +4 V under small FB (S-FB), large FB (L-FB) and RB, respectively. A circle delineates the S value at T = 10 K. (c) ln(I_{DS}/V_{DS}^2)–1/V_{DS} plot of the I_{DS}–V_{DS} curves with V_{BG} = +4 V at 50, 100 and 300 K, respectively. A circle indicates the deviation between measured and calculated data. Inset: schematic energy band diagrams for S-RB and L-RB, respectively. The rhombs represent the tunneling barrier at junction interface due to nanosize gap or adsorbents.

$\ln\left(\frac{I_{DS}}{V_{DS}^2}\right) \propto \ln\left(\frac{1}{V_{DS}}\right)$ for the linear and nonlinear regimes, respectively, are also shown for comparison. One can see that the measured values fit the calculation results well at 50 and 100 K. The consistency suggests that the charge transport experiences a transition from direct to F–N tunneling at V_t. It is worth noting that the measurement results deviate from the calculated curve in the nonlinear regime at 300 K (circle). The reason could be the thermionic emission component becomes nonnegligible at 300 K. The physic pictures of the transport mechanisms are illustrated in the inset. The RB bias increases the potential barrier, leading to the suppressed current. At a small RB (S-RB), the voltage across the junction barrier (dotted rhomb) is small. Thus the majority of holes tunnel through a rectangular barrier. In contrast, the voltage across the junction barrier increases when RB voltage is increased. Most of the holes injected from D have to tunnel through the triangular junction barrier due to the increased potential barrier (path *a*). Alternatively, as the barrier in depletion region becomes thinner, holes might recombine with electrons from D through the interface states owing to the imperfect junction (path *b*) [28]. One can see that in both case *a* and *b*, tunneling current dominates the transport.

4. Conclusions

A single-walled carbon nanotube based intermolecular p–n junction is demonstrated through contacting the SWCNT channels of p- and n-type CNTFETs. Current rectification characteristics largely depend on the back-gate voltage. At a small forward bias, thermionic emission is the dominant transport mechanism. On the contrary, at a large forward bias or reverse bias, the tunneling transport is more important. It is also found that the transport mechanism experiences a transition from direct tunneling to Fowler–Nordheim tunneling through the junction barrier at the cross of the p- and n-type CNT channels.

Acknowledgement

This work was supported by Temasek Laboratory and Ministry of Education of Singapore.

References

[1] Zhou C, Kong J, Yenilmez E, Dai H. Modulated chemical doping of individual carbon nanotubes. Science 2000;290:1552–5.
[2] Lee JU, Gipp PP, Heller CM. Carbon nanotube p–n junction diodes. Appl Phys Lett 2004;85:145–7.
[3] Fuhrer MS, Nygård J, Shih L, Forero M, Yoon YG, Mazzoni MSC, et al. Crossed nanotube junctions. Science 2000;288:494–7.
[4] Papadopoulos C, Rakitin A, Li J, Vedeneev AS, Xu JM. Electronic transport in Y-junction carbon nanotubes. Phys Rev Lett 2000;85:3476–9.
[5] Choi YC, Choi W. Synthesis of Y-junction single-wall carbon nanotubes. Carbon 2005;43:2737–41.
[6] Wei D, Liu Y, Cao L, Fu L, Li X, Wang Y, et al. A new method to synthesize complicated multibranched carbon nanotubes with controlled architecture and composition. Nano Lett 2006;6:186–92.
[7] Kim J, Kim J-R, Lee JO, Park JW, So HM, Kim N, et al. Fano resonance in crossed carbon nanotubes. Phys Rev Lett 2003;90:1664031-1–31-4.
[8] Tombler TW, Zhou C, Kong J, Dai H. Gating individual nanotubes and crosses with scanning probes. Appl Phys Lett 2000;76:2412–4.
[9] Gao B, Komnik A, Egger R, Glattli DC, Bachtold A. Evidence for Luttinger-Liquid behavior in crossed metallic single-wall nanotubes. Phys Rev Lett 2004;92:2168041-1–41-4.
[10] Postma HWC, De Jonge M, Yao Z, Dekker C. Electrical transport through carbon nanotube junctions created by mechanical manipulation. Phys Rev B 2000;62:R10653–6.
[11] Li H, Zhang Q. Tunable ambipolar Coulomb blockade characteristics in carbon nanotube-gated carbon nanotube field-effect transistors. Appl Phys Lett 2009;94:022101-1–1-3.
[12] Collins PG, Bradley K, Ishigami M, Zettl A. Extreme oxygen sensitivity of electronic properties of carbon nanotubes. Science 2000;287:1801–4.
[13] Kang D, Park N, Ko JH, Bae E, Park W. Oxygen-induced p-type doping of a long individual single-walled carbon nanotube. Nanotechnology 2005;16:1048–52.
[14] Ahn YH, Tsen AW, Kim B, Park YW, Park J. Photocurrent imaging of p–n junctions in ambipolar carbon nanotube transistors. Nano Lett 2007;7:3320–3.
[15] Derycke V, Martel R, Appenzeller J, Avouris Ph. Controlling doping and carrier injection in carbon nanotube transistors. Appl Phys Lett 2002;80:2773–5.
[16] Kaminishi D, Ozaki H, Ohno Y, Maehashi K, Inoue K, Matsumoto K, et al. Air-stable n-type carbon nanotube field-effect transistors with Si_3N_4 passivation

films fabricated by catalytic chemical vapor deposition. Appl Phys Lett 2005;86:1131151-1–51-3.
[17] Li H, Zhang Q, Marzari N. Global and local charge trapping in carbon nanotube field-effect transistors. Nanotechnology 2008;19:1752031-1–31-5.
[18] Jhi SH, Louie SG, Cohen ML. Electronic properties of oxidized carbon nanotubes. Phys Rev Lett 2000;85:1710–3.
[19] Appenzeller J, Radosavljević M, Knoch J, Avouris Ph. Tunneling versus thermionic emission in one-dimensional semiconductors. Phys Rev Lett 2004;92:048301-1–1-4.
[20] Li H, Zhang Q, Marzari N. Unique carbon-nanotube field-effect transistors with asymmetric source and drain contacts. Nano Lett 2008;8:64–8.
[21] Yamada T. Modeling of carbon nanotube Schottky barrier modulation under oxidizing conditions. Phys Rev B 2004;69:1254081-1–81-8.
[22] Li H, Loke WK, Zhang Q, Yoon SF. Physical device modeling of carbon nanotube/GaAs photovoltaic cells. Appl Phys Lett 2010;96:043501-1–1-3.
[23] Martel R, Derycke V, Lavoie C, Appenzeller J, Chan KK, Tersoff J, et al. Ambipolar electrical transport in semiconducting single-walled carbon nanotubes. Phys Rev Lett 2001;87:2568051-1–51-4.
[24] Kim DH, Huang J, Shin H-K, Roy S, Choi W. Transport phenomena and conduction mechanism of single-walled carbon nanotubes (SWNTs) at Y- and crossed-junctions. Nano Lett 2006;6:2821–5.
[25] Riben AR, Feucht DL. nGe-pGaAs heterojunctions. Solid-State Electron 1966;9:1055–65.
[26] Simmons JG. Generalized formula for the electric tunnel effect between similar electrodes separated by a thin insulating film. J Appl Phys 1963;34:1793–803.
[27] Chiu PW, Roth S. Transition from direct tunneling to field emission in carbon nanotube intramolecular junctions. Appl Phys Lett 2008;92:0421071-1–71-3.
[28] Anderson RL. Experiments on Ge–GaAs heterojunctions. Solid-State Electron 1962;5:341–51.